Magic
Defects

Capacitance

MATERIALS
CHEMISTRY
FRONTIERS

Check for updates

Exploring the microscopic mechanism of pseudocapacitance with electronic structures in monolayer 1T-MoS₂ electrodes for supercapacitors†

Zhenzhou Zhang,[a] Maokun Wu,[a] Lijing Wang,[a] Jin Wang,[a] Yahui Cheng, [iD][a] Luyan Li,[b] Hong Dong,[a] Hui Liu,[a] Zhanglian Hong,[c] Kyeongjae Cho, [iD][ad] Feng Lu,[a] Weichao Wang [iD]*[a] and Wei-Hua Wang [iD]*[a]

Quasi-two-dimensional 1T-MoS₂ is a promising pseudocapacitance (C_{redox}) electrode material due to its large specific surface area, superior electrical conductivity and mechanical stability. However, the microscopic mechanism of C_{redox} and its further manipulation *via* modulating the structures and electronic structures are still unclear. Thus, the C_{redox} of monolayer 1T-MoS₂ has been explored based on first-principles calculations. For monolayer 1T-MoS₂ adsorbed by H^+ ions on one side or both sides, a band gap opens, decreases and even disappears with the coverage increase in H^+ ions up to 100%. In this process, the charge transfer from the monolayer 1T-MoS₂ to the adsorbed H^+ ions almost linearly increases with the coverage increase in the H^+ ions. In contrast, the potential change rate of the monolayer 1T-MoS₂ reduces, resulting in the enhancement of C_{redox}. Herein, the maximum values of C_{redox} reached $\sim$76.7 $\mu F\ cm^{-2}$ (252.8 F g^{-1}) and $\sim$213.7 $\mu F\ cm^{-2}$ (704.5 F g^{-1}) for the 100% coverage of H^+ ions on one side and both sides, respectively. Furthermore, the manipulation of C_{redox} in the monolayer 1T-MoS₂ could be realized through intrinsic defects engineering. Particularly, the C_{redox} was greatly improved in the system with S vacancies. These results would provide significantly fundamental insights for understanding the correlation between the C_{redox} and the electronic structures of 1T-MoS₂ and other similar quasi-two dimensional materials.

Introduction

With the exhaustion of fossil resources and serious environmental pollution issues, exploiting environmentally friendly and renewable resources is an effective strategy to solve this problem. Among these solving schemes, it is significant to design highly efficient energy conversion and storage systems.[1–6] Nowadays, lithium-ion batteries and supercapacitors are two types of energy storage systems widely applied in electrical/hybrid vehicles and portable devices. Lithium-ion batteries can provide large energy density, *e.g.* 120–170 W h kg^{-1}, due to their high redox potential of Faraday energy storage mechanism. Nevertheless, lithium-ion batteries cannot provide huge energy in a short time to meet the demands of high power devices due to their slower kinetic Faraday process.[7] In contrast, supercapacitors have been extensively studied due to their high power density, fast charging–discharging rate, long cyclic lifetime, low maintenance cost, *etc.*[8–10] However, the current energy density of the supercapacitors is only limited to 5–10 W h kg^{-1}.[11] Therefore, it is required and currently urgent to improve the energy density of supercapacitors while maintaining their large power density output.

In order to enhance the energy density of the supercapacitors, improving the specific capacitance of electrodes is one of the important routes. According to the energy storage mechanisms, the supercapacitors are generally divided into two types, namely electrical double layer capacitance (EDLC) and pseudocapacitance (C_{redox}). Remarkably, it is pointed out that the C_{redox} is one to two orders of magnitude higher than EDLCs in most of the present supercapacitors.[12] As suitable electrode materials for supercapacitors, it is expected to possess large specific surface area, excellent electrical conductivity, mechanical stability and highly redox reaction activity. Since the discovery of graphene,[13]

[a] *Department of Electronic Science and Engineering, and Tianjin Key Laboratory of Photo-Electronic Thin Film Device and Technology, Nankai University, Tianjin, 300071, P. R. China. E-mail: whwangnk@nankai.edu.cn, weichaowang@nankai.edu.cn*

[b] *School of Science, Shandong Jianzhu University, Jinan, 250101, China*

[c] *State Key Laboratory of Silicon Materials, School of Materials Science and Engineering, Zhejiang University, Hangzhou, 310027, China*

[d] *Department of Material Science and Engineering, the University of Texas at Dallas, Richardson, 75080, USA*

† Electronic supplementary information (ESI) available. See DOI: 10.1039/c9qm00060g

graphene and graphene-like quasi-two-dimensional materials, such as transition metal dichalcogenides (TMDs), graphdiyne, transition metal carbides and carbonitrides (MXenes) have been widely used in electrode materials and photoelectrocatalysts due to their large specific surface area, superior electrical conductivity and good mechanical properties.[14–18] It is noted that the C_{redox} or electrochemical performance of graphene and its derivatives could be improved only after introducing intrinsic defects and external dopings, or by combining with transition metal compounds.[19–24] The C_{redox} of two-dimensional metal carbides or nitrides is also influenced by surface functional groups dependent on experimental conditions of etching preparations.[25–28]

Monolayer or few layers TMDs, represented by MoS_2, have similar structures to graphene and can be well-prepared in experiments. Particularly, MoS_2 with 1T structure is metallic and it has been applied as electrode materials. For instance, Zhu *et al.* demonstrated that the capacitance of multilayer 1T-MoS_2 in aqueous condition is up to 380 F g^{-1} at a scan rate of 5 mV s^{-1}.[29] Chhowalla *et al.* displayed that the capacitance of exfoliated 1T-MoS_2 nanosheets ranges from 400 F cm^{-3} to 700 F cm^{-3} in aqueous electrolytes.[30] In fact, the adsorption of the ions on electrodes not only changes the charge filling of the energy bands but also influences the electronic structures of the electrodes.[31,32] Although considerable experimental progress has been achieved for 1T-MoS_2 as electrodes, the microscopic mechanism of the C_{redox} and the manipulation of C_{redox} *via* modulating the structures and electronic structures are still inaccessible.

In this study, the microscopic mechanism of C_{redox} with the electronic structures was investigated. We found that the charge transfer almost linearly increased with the increase in the H$^+$ ions coverage on one side and both sides of the monolayer 1T-MoS_2. The C_{redox} was dependent on the potential change to a large extent during the process of the H$^+$ ions adsorption. The maximum C_{redox} was achieved at the 100% H$^+$ coverage and further improvements could be realized by introduction of the intrinsic S vacancies. These results clarified the correlation between the C_{redox} and the electronic structures of monolayer 1T-MoS_2 and would also provide fundamental insights for the further manipulation of C_{redox} in 1T-MoS_2 and other similar 2D materials.

Computational model and details

Our calculations were performed within the Vienna ab initio simulation package (VASP) based on the plane wave basis method.[33] For the exchange correlation potential, generalized gradient approximation (GGA) with Perdew–Burke–Ernzerhof (PBE) functional was adopted.[34] To simulate the C_{redox} of 1T-MoS_2, a 3 × 3 supercell was adopted, as shown in Fig. 1. The energy cutoff of plane wave was set to be 400 eV. The Monkhorst–Pack *k*-point grids of 5 × 5 × 1 and 9 × 9 × 1 were used for structural optimizations and self-consistent electronic structures, respectively. The optimized structure was obtained until the residual force on each atom converged to less than 0.02 eV Å^{-1}. In the electronic
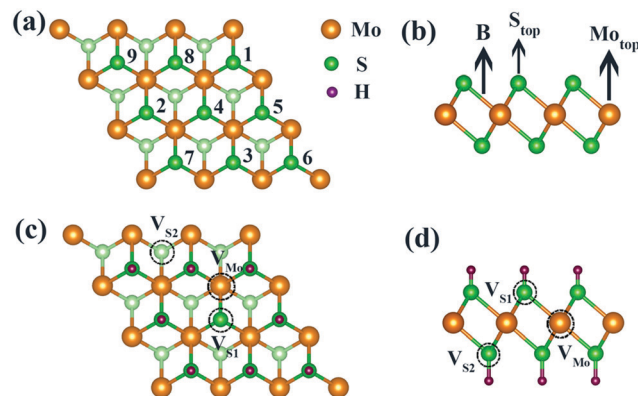

Fig. 1 (a) Top view and (b) side view of monolayer 1T-MoS_2 with a layered structure. The orange, green and light green spheres represent Mo atoms, the top layer S and the bottom layer S atoms, respectively. The adsorption sites with the increase in the H$^+$ ions coverage are labelled by numbers. (c) Top view and (d) side view of possible intrinsic vacancies: S vacancies at top layer, V_{S1}, or bottom layer, V_{S2}, and Mo vacancy, V_{Mo}.

structures steps, the energy was converged to less than 10^{-5} eV. In order to minimize the interaction between the vertically periodic layers, the thickness of the vacuum layer was set to be 20 Å along the z direction.

Results and discussion

Structural configurations and stabilities of H$^+$ ions adsorbed on monolayer 1T-MoS_2

Monolayer 1T-MoS_2 exhibits a sandwiched structure, where Mo atoms are sandwiched between two layers of S atoms, as shown in Fig. 1(b). The monolayer MoS_2 has two different coordinated structures, namely trigonal phase (1T) and hexagonal phase (H).[35,36] Compared with the H phase, the 1T-MoS_2 prepared by the lithium ion intercalation and hydrothermal method exhibits superior electrical conductivity and structural stability even up to 100 °C.[32,37,38] In this study, the monolayer 1T-MoS_2 is our focus. The optimized lattice constant of 1T-MoS_2 unit cell is 3.18 Å and the bond length of Mo–S is 2.42 Å, which is well consistent with the experimental data and previous reports.[39–41]

In order to unveil the mechanism of C_{redox} in aqueous conditions, the model system of H$^+$ ions adsorbed on the surface of monolayer 1T-MoS_2 was adopted. The total adsorbed system was in the neutral state since the equally additional number of electrons supplied to 1T-MoS_2 would compensate the H$^+$ ions in the charging state of supercapacitors. The adsorption energy (E_{ad}) of H$^+$ ions on 1T-MoS_2 is defined as:

$$E_{ad} = (E_{tot} - E_{pristine} - nE_H)/n \qquad (1)$$

where E_{tot}, $E_{pristine}$, and E_H are the energies of total 1T-MoS_2-H supercell, pristine 1T-MoS_2 supercell, and one hydrogen atom, respectively, and n is the number of the adsorbed H$^+$ ions. According to formula (1), the more negative the E_{ad}, the more stable the adsorbed system is.

For one specific H$^+$ ion adsorbed on monolayer 1T-MoS_2, three configurations of top site above S atom (S_{top}), top site
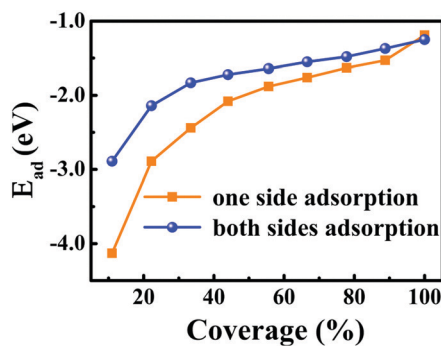
Fig. 2 Dependence of the adsorption energies of H^+ ions on one side and both sides of 1T-MoS$_2$ on the H^+ ions coverage. The corresponding relationship between the coverage and the number of the adsorbed H^+ ions are listed in Table S1 of ESI.†

above Mo atom (Mo$_{top}$) and bridge site above S–Mo bond (B) are displayed in Fig. 1(b). The adsorption energies of S$_{top}$, Mo$_{top}$ and B site are -4.13 eV, -2.41 eV and -3.75 eV, respectively, indicating the favourable S$_{top}$ adsorption for H^+ ions. For two H^+ ions adsorbed on one side of monolayer 1T-MoS$_2$, two possible configurations of the nearest neighbouring (NN) and next nearest neighbouring adsorptions existed based on the distance between these two H^+ ions. Through comparing the E_{ad} of the NN and NNN configurations, we found that the NNN adsorption was more stable with an energy difference of 0.15 eV. With the increase in the adsorbed H^+ ions, the possible configurations and the E_{ad} were also examined, as shown in Table S1 of the ESI.† The most stable adsorbed sites are labelled by numbers in Fig. 1(a) according to the coverage

increase in the H^+ ions. It can be seen that the H^+ ions tend to distribute away from each other to minimize the coulomb repulsions among them when the coverage is not large. To provide references for experiments, the coverage is used and defined as the ratio of the adsorbed H^+ ions amount to the total active S$_{top}$ sites. As the coverage increases, the absolute values of E_{ad} gradually decrease but always with negative values in Fig. 2, implying the stable adsorbed state up to 100% coverage.

Besides the one side adsorption of H^+ ions on 1T-MoS$_2$, both sides adsorption is reasonable to improve the C_{redox} in practical nano array electrodes.[42–46] Through comparing the E_{ad} for different adsorbed configurations, it is seen that the symmetrically adsorbed configurations between the top and the bottom S layers are favourable. As displayed in Fig. 2, the E_{ad} of H^+ ions on both sides also follows the similar character except for slightly weaker than that of the one side adsorption, which is basically induced by the stronger coulomb repulsions among more adsorbed H^+ ions.

Electronic structures of the H^+ ions adsorption on monolayer 1T-MoS$_2$

For supercapacitor electrodes, the fast charge/discharge rate is closely related to the carrier conductivity, which is reflected by the electronic structures of the electrode materials. For one side H^+ adsorption of monolayer 1T-MoS$_2$, the density of states (DOS) and partial DOS (PDOS) of monolayer 1T-MoS$_2$ under the different adsorption coverages of H^+ ions are presented in Fig. 3. The evolution of band structures with the H^+ coverage is also provided in Fig. S1 of ESI.† In Fig. 3(a), the pristine monolayer 1T-MoS$_2$ shows metallic character, which is consistent with the previous report.[39] The states near the Fermi level (E_F) are
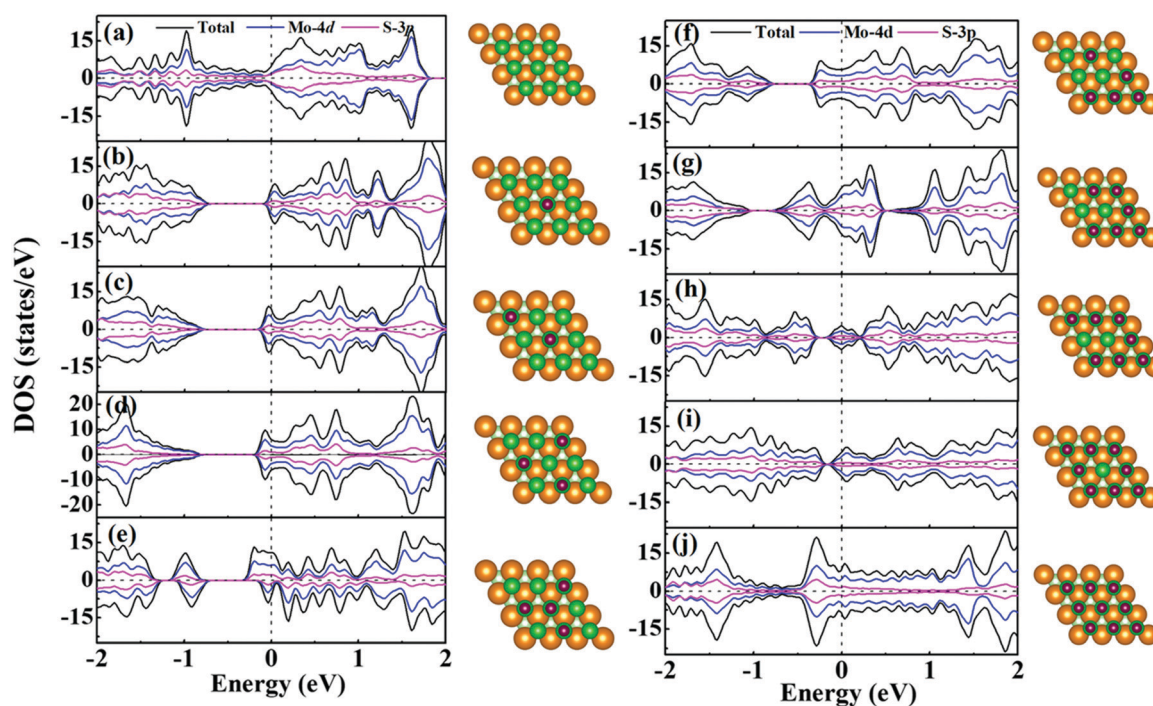

Fig. 3 Total DOS, PDOS and geometric structures of 1T-MoS$_2$ under different adsorption coverage of H^+ ions on one side of 1T-MoS$_2$. Pristine 1T-MoS$_2$ in (a), and the coverage is 11.1% in (b), 22.2% in (c), 33.3% in (d), 44.4% in (e) 55.6% in (f) 66.7% in (g) 77.8% in (h), 88.9% in (i), 100% in (j). The Fermi level is set to be 0.0 eV.

1312 | *Mater. Chem. Front.*, 2019, **3**, 1310–1316

This journal is © The Royal Society of Chemistry and the Chinese Chemical Society 2019

basically contributed by Mo-4d and S-3p orbitals due to the p–d hybridizations. When the active S_{top} sites on one side of monolayer 1T-MoS$_2$ partially adsorb the H$^+$ ions, the monolayer 1T-MoS$_2$ opens one band gap and the band gap value decreases with the increment in the H$^+$ coverage in Fig. 3(b–i). Under these situations, the E_F is located within the conduction band, and the monolayer 1T-MoS$_2$ still displays the metallic-like character. It is noted that the monolayer 1T-MoS$_2$ demonstrates excellent metallic properties under the full coverage of H$^+$ ions in Fig. 3(j) and Fig. S1(i) (ESI†). For monolayer 1T-MoS$_2$ with H$^+$ ions adsorbed on both sides, the DOS, PDOS and band structures of the 1T-MoS$_2$ under different adsorption coverages are shown in Fig. S2 and S3 (ESI†). It is found that the monolayer 1T-MoS$_2$ with both sides adsorption also shares the similar character to that with one side adsorption. Particularly, the metallic band structures of monolayer 1T-MoS$_2$ are well preserved at 100% coverage of H$^+$ ions in Fig. S3(i) (ESI†). Combined with the practical applications, the larger adsorption coverage of H$^+$ ions and the excellent electrical conductivity are desirable to induce the promising large C_{redox} for monolayer 1T-MoS$_2$.

Since the C_{redox} is associated with the charge transfer between the adsorbed ions and the electrode, the charge density difference $\Delta\rho$ is presented in Fig. 4 to more vividly observe the charge transfer between the H$^+$ ions and the charging monolayer 1T-MoS$_2$. $\Delta\rho$ is expressed as

$$\Delta\rho = \rho(\text{MoS}_2 - n\text{H}) - \rho(\text{MoS}_2{}^{n-}) - \rho(n\text{H}^+) \qquad (2)$$

where $\rho(\text{MoS}_2 - n\text{H})$, $\rho(\text{MoS}_2{}^{n-})$ and $\rho(n\text{H}^+)$ are the electron densities of 1T-MoS$_2$–nH systems, the charging monolayer 1T-MoS$_2$ and the isolated H$^+$ ions.

As shown in Fig. 4, the monolayer 1T-MoS$_2$ donates electrons to H$^+$ ions in all coverage cases. In detail, the localized charge transfer basically occurs between the H$^+$ ions and adjacent Mo atoms in the lower coverage systems. With the coverage increase in the H$^+$ ions, the charge density difference distribution tends

to be delocalized within 2D sheet of 1T-MoS$_2$, indicating the improvement in the metallic properties for monolayer 1T-MoS$_2$. In particular, the charge density difference in Fig. 4(i) is almost uniformly distributed in the 2D plane of the monolayer 1T-MoS$_2$, consistent with the metallic band structures of 1T-MoS$_2$ with 100% coverage of H$^+$ ions in Fig. 3(j).

Pseudocapacitance of H$^+$ ions adsorption on monolayer 1T-MoS$_2$

Due to the fast reversible adsorption/desorption process of H$^+$ ions in supercapacitors, the electrode of monolayer 1T-MoS$_2$ would gain electrons to saturate the positive charges of H$^+$ ions in the charging state. The C_{redox} induced in this process can be calculated by

$$C_{redox} = \Delta Q / \Delta V \qquad (3)$$

where ΔQ and ΔV are the charge transfer from the electrode to H$^+$ ions and the potential change of the electrode, respectively. ΔQ can be obtained based on the Bader charge analysis and the potential change in monolayer 1T-MoS$_2$ is estimated by work function (WF) change:

$$\Delta V = \Delta\text{WF}/e \qquad (4)$$

$$\Delta\text{WF} = \text{WF}_{\text{MoS}_2 - n\text{H}} - \text{WF}_{\text{MoS}_2{}^{\Delta Q-}} \qquad (5)$$

where $\text{WF}_{\text{MoS}_2 - n\text{H}}$ and $\text{WF}_{\text{MoS}_2{}^{\Delta Q-}}$ are the work functions of the monolayer 1T-MoS$_2$ adsorbed H$^+$ ions at neutral state and the charged monolayer 1T-MoS$_2$ with negative charge of ΔQ, respectively. For monolayer 1T-MoS$_2$ itself, its E_F crosses the energy bands and it is metallic whether in the pristine state or in charging state with additional negative charges through external circuit, as demonstrated by the uniformly distributed charges on the 2D plane of 1T-MoS$_2$ in Fig. S4 of ESI.† Thus, the WF of monolayer 1T-MoS$_2$ in charging state is accessible via the shift of E_F (ΔE_F) relative to pristine 1T-MoS$_2$ according to the rigid-band approximation, which is presented in Fig. S5 of ESI.†
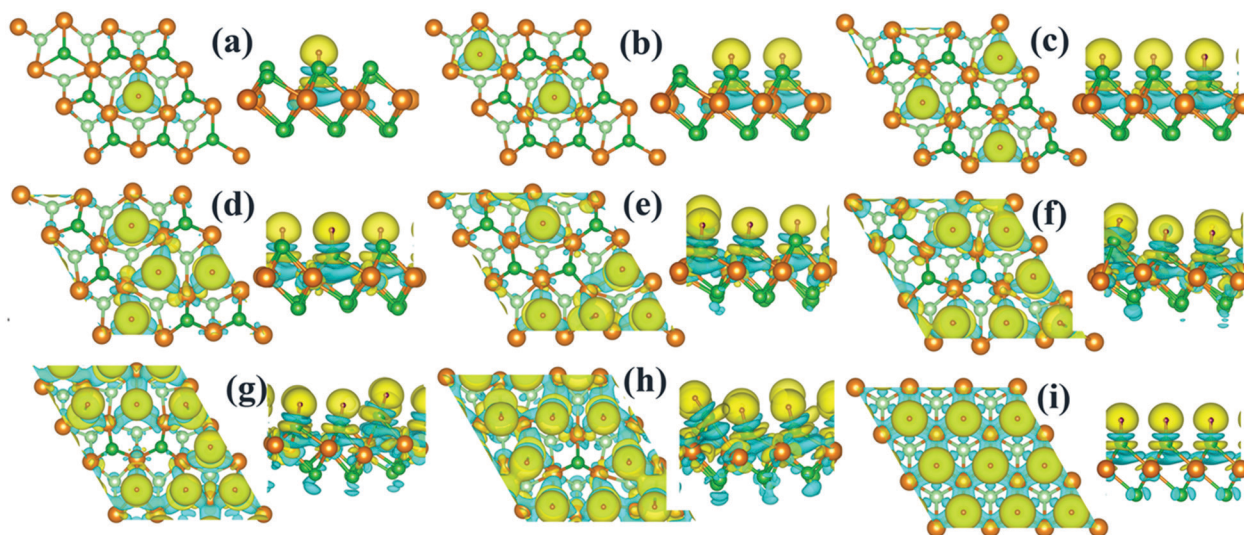

Fig. 4 Top and side views of charge density difference distribution. The coverage is 11.1% in (a), 22.2% in (b), 33.3% in (c), 44.4% in (d) 55.6% in (e) 66.7% in (f) 77.8% in (g), 88.9% in (h), and 100% in (i). The yellow and cyan isosurfaces with an isovalue of 0.003 e Å^{-3} correspond to charge accumulation and depletion, respectively.

This journal is © The Royal Society of Chemistry and the Chinese Chemical Society 2019

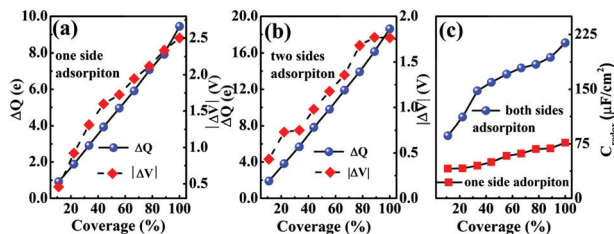*Mater. Chem. Front.*, 2019, **3**, 1310–1316 | **1313**

Fig. 5 Charge transfer and potential change at different H^+ ion coverages on one side (a) and on both sides (b) of monolayer 1T-MoS$_2$. Pseudocapacitance corresponding to (a) and (b) is presented in (c).
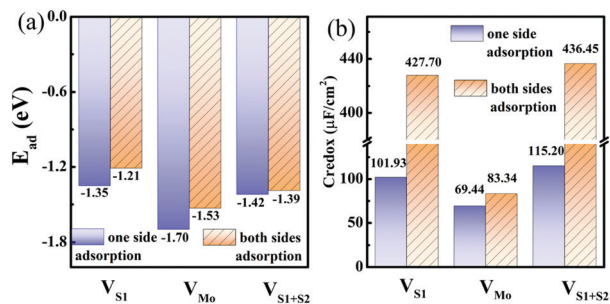

Fig. 6 (a) Adsorption energies and (b) pseudocapacitance of monolayer 1T-MoS$_2$ with 100% coverage of H^+ ions on one side and both sides under different intrinsic defect states.

In Fig. 5(a and b), it is seen that the charge transfer, ΔQ, from the charged electrode to the H^+ ions increases almost linearly with the increase in the coverage of H^+ ions on one side or both sides of monolayer 1T-MoS$_2$. At the same time, the WF values of monolayer 1T-MoS$_2$ adsorbed by H^+ ions at neutral state, WF_{MoS_2-nH}, and monolayer 1T-MoS$_2$ with negatively charges, $WF_{MoS_2^{\Delta Q^-}}$, gradually decrease, which are listed in Table S2 of ESI.† The former is associated with the charge transfer and the surface electrical dipole,[47] and the latter is related to ΔE_F of the charged 1T-MoS$_2$ relative to pristine 1T-MoS$_2$. Due to the extended DOS near the E_F of monolayer 1T-MoS$_2$, ΔE_F slightly increases with the increase in the electrons gain, leading to a slow reduction in $WF_{MoS_2^{\Delta Q^-}}$. Hence, the potential change is related to the work function variation of monolayer 1T-MoS$_2$ after adsorption by H^+ ions. As the rate of decrease in WF_{MoS_2-nH} gets slower with the increase in the H^+ ions coverage, particularly close to the complete coverage, the maximum values of the C_{redox}, ~ 76.67 μF cm^{-2} (~ 252.81 F g^{-1}) for one side adsorption and ~ 213.67 μF cm^{-2} (704.53 F g^{-1}) for two sides adsorption, respectively, have been obtained in Fig. 5(c). Our theoretically obtained C_{redox} is higher than the reported experimental data, and further improvement of C_{redox} would be expected and promising in experiments.[29,48,49]

Pseudocapacitance manipulation of monolayer 1T-MoS$_2$ by intrinsic defects

The maximum C_{redox} of monolayer 1T-MoS$_2$ is achieved at full coverage of H^+ ions due to the well-preserved structures and metallic electronic structures of monolayer 1T-MoS$_2$. Combined with the experiments, the intrinsic defects of S vacancies or Mo vacancies possibly exist in the growth process due to different preparation conditions.[50–53] To illustrate the influence of the defects on the C_{redox} and to further manipulate C_{redox} through introducing defects conversely, the effects of possible vacancies are explored in 100% coverage of H^+ ions on monolayer 1T-MoS$_2$. As shown in Fig. 1(c and d), for the 3×3 supercell with 100% coverage of H^+ ions on one side and on both sides, one Mo vacancy (V_{Mo}), one S vacancy (V_{S1}), and two S vacancies in top and bottom layers ($V_{S1} + V_{S2}$) are considered. Under this situation, the E_{ad} of H^+ ions is expressed as,

$$E_{ad} = (E_{tot} - E_{defect} - nE_H)/n \qquad (6)$$

where E_{tot}, E_{defect}, and E_H are the energies of the defective 1T-MoS$_2$–nH system, the defective 1T-MoS$_2$ system, and one

hydrogen atom, respectively. Moreover, $n = 9$ or $n = 18$ corresponds to the 100% coverage of H^+ ions on one side or both sides of monolayer 1T-MoS$_2$.

With the intrinsic defects in 1T MoS$_2$–nH system, the E_{ad} of H^+ ions is still negative for one side and both sides adsorption cases in Fig. 6(a), implying the energetically stable adsorption of H^+ ions on defect monolayer 1T-MoS$_2$. Moreover, the adsorption of H^+ ions on 1T-MoS$_2$ in the presence of V_{S1}, V_{Mo}, or V_{S1+S2} gets slightly stronger than that on pristine 1T-MoS$_2$, which is resulted from the nearest H^+ moving closer to the vacancy site and the enhanced interaction between the H^+ and the 1T-MoS$_2$. In Fig. 6(a), it is also found that the adsorption of H^+ ions on one side is more stable than that on both sides owing to the stronger Coulomb repulsion interaction between more H^+ ions adsorbed on both sides of monolayer 1T-MoS$_2$. In terms of the DOS in Fig. S6 of ESI,† all the above-mentioned systems demonstrate metallic characters, which could ensure the defective monolayer 1T-MoS$_2$ possesses the well rate performance as an electrode.

In the presence of S vacancies, the C_{redox} is increased to 101.93 μF cm^{-2} (336.09 F g^{-1}) and 115.20 μF cm^{-2} (379.83 F g^{-1}) in 100% coverage of H^+ ions on one side of monolayer 1T-MoS$_2$ with V_{S1} and V_{S1+S2}, respectively, as shown in Fig. 6(b). Furthermore, the C_{redox} in 100% coverage of H^+ ions on both sides of monolayer 1T-MoS$_2$ system is enhanced to 427.70 μF cm^{-2} (1410.24 F g^{-1}) and 436.45 μF cm^{-2} (1439.08 F g^{-1}) when V_{S1} and V_{S1+S2} are included. It is observed from Table S4 (ESI†) that the WF_{MoS_2-nH} of the system with S vacancies with respect to that of the intrinsic system is increased, which is induced by more electrons transfer from the defect 1T-MoS$_2$ to H^+ ions. At the same time, $WF_{MoS_2^{\Delta Q^-}}$ of monolayer 1T-MoS$_2$ with S vacancies at charging state is suppressed relative to that of the pristine 1T-MoS$_2$ since the S vacancies contribute more electrons to facilitate the electrons emission. Thus, the potential difference, ΔV, is also suppressed, leading to an increased C_{redox} in Fig. 6(b).

In contrast, the presence of the V_{Mo} reduces the C_{redox} of monolayer 1T-MoS$_2$. For instance, the C_{redox} of the systems with one-side adsorption and two-side adsorption of H^+ ions are 69.44 μF cm^{-2} and 83.34 μF cm^{-2}, respectively, while the corresponding values are 76.67 μF cm^{-2} and 213.67 μF cm^{-2} in pristine systems with the same H^+ ion coverage. As indicated

1314 | *Mater. Chem. Front.*, 2019, **3**, 1310–1316

This journal is © The Royal Society of Chemistry and the Chinese Chemical Society 2019

in Table S4 (ESI†), the V_{Mo} lifts the WF of pristine monolayer 1T-MoS$_2$ $\left(WF_{MoS_2^{\Delta Q^-}}\right)$ and simultaneously suppresses the WF of the total system (WF_{MoS_2-nH}), generating a larger potential difference between them and a decreased C_{redox}. Through looking into the effects of the intrinsic defects on the C_{redox} of monolayer 1T-MoS$_2$, the C_{redox} would be manipulated and improved to a large extent by controlling the experimental growth conditions in S poor environment to produce S vacancies.

In addition, about the approach to calculate the C_{redox}, C_{redox} is directly dependent on ΔQ and ΔV, which can be applied in other 2D materials and oxides. ΔQ is acquired by the charge transfer based on Bader charge analysis, and ΔV is obtained by the work function change of the electrode material. In other electrodes materials, the stability of the adsorbed systems, the charge transfer between the electrodes and the adsorbed ions, and the work function change are possibly different from monolayer 1T-MoS$_2$ system. Particularly, the optimal performance of C_{redox} and the favourable coverage of H$^+$ ions need to be further examined.

Conclusions

In summary, the correlation between the C_{redox} and the microscopic electronic structures was examined based on the DFT calculations. One factor determining the C_{redox} is the charge transfer from the electrode to the adsorbed H$^+$ ions. The other is the potential change of the electrode due to the H$^+$ ions adsorption. For pristine monolayer 1T-MoS$_2$, the amount of the charge transfer increases almost linearly with the increase in the H$^+$ ion coverage. Thus, the C_{redox} is mainly dependent on the potential change of the monolayer 1T-MoS$_2$. The smaller decrease rate of the potential change in monolayer 1T-MoS$_2$ with fully coverage of H$^+$ ions on both sides results in a higher C_{redox} of 213 μF cm^{-2} (704 F g^{-1}). Moreover, the C_{redox} is much improved after introducing S vacancies. These results would provide theoretical guidance in understanding and manipulating the pseudocapacitance properties of 1T-MoS$_2$ or other similar quasi-two-dimensional materials for further experimental explorations.

Author contributions

Wei-Hua Wang and Weichao Wang proposed the research idea, wrote and reviewed the manuscript. Zhenzhou Zhang performed the calculations and wrote the draft. Maokun Wu, Lijing Wang and Jin Wang did part of calculations. All the authors devoted to the discussions and revised the manuscript.

Conflicts of interest

There are no conflicts to declare.

Acknowledgements

References

1 L. F. Chen, Y. Feng, H. W. Liang, Z. Y. Wu and S. H. Yu, *Adv. Energy Mater.*, 2017, **7**, 1700826.

2 C. P. Grey and J. M. Tarascon, *Nat. Mater.*, 2017, **16**, 45–56.

3 G. Zhang, Y. Han, C. Shao, N. Chen, G. Sun, X. Jin, J. Gao, B. Ji, H. Yang and L. Qu, *Mater. Chem. Front.*, 2018, **2**, 1750.

4 N. Choudhary, M. A. Islam, J. H. Kim, T. J. Ko, A. Schropp, L. Hurtado, D. Weitzman, L. Zhai and Y. Jung, *Nano Today*, 2018, **19**, 16–40.

5 N. Yang, Y. Zhang, J. E. Halpert, J. Zhai, D. Wang and L. Jiang, *Small*, 2012, **8**, 1762–1770.

6 Y. Zhao, H. Tang, N. Yang and D. Wang, *Adv. Sci.*, 2018, **5**, 1800959.

7 F. Wang, X. Wu, X. Yuan, Z. Liu, Y. Zhang, L. Fu, Y. Zhu, Q. Zhou, Y. Wu and W. Huang, *Chem. Soc. Rev.*, 2017, **46**, 6816–6854.

8 R. Li, Y. Wang, C. Zhou, C. Wang, X. Ba, Y. Li, X. Huang and J. Liu, *Adv. Funct. Mater.*, 2015, **25**, 5384–5394.

9 F. Yu, T. Wang, Z. Wen and H. Wang, *J. Power Sources*, 2017, **364**, 9–15.

10 H. Wang, C. M. B. Holt, Z. Li, X. Tan, B. S. Amirkhiz, Z. Xu, B. C. Olsen, T. Stephenson and D. Mitlin, *Nano Res.*, 2012, **5**, 605–617.

11 C. Liu, Z. Yu, D. Neff, A. Zhamua and B. Z. Jang, *Nano Lett.*, 2010, **10**, 4863–4868.

12 B. E. Conway, *J. Electrochem. Soc.*, 1991, **138**, 1539.

13 K. S. Novoselov, A. K. Geim, S. V. Morozov, D. Jiang, Y. Zhang, S. V. Dubonos, I. V. Grigorieva and A. A. Firsov, *Science*, 2004, **306**, 666–669.

14 N. Yang, J. Zhai, D. Wang, Y. Chen and L. Jiang, *ACS Nano*, 2010, **2**, 887–894.

15 H. Ren, H. Shao, L. Zhang, D. Guo, Q. Jin, R. Yu, L. Wang, Y. Li, Y. Wang, H. Zhao and D. Wang, *Adv. Energy Mater.*, 2015, **5**, 1500296.

16 Y. Zhao, J. Wan, H. Yao, L. Zhang, K. Lin, L. Wang, N. Yang, D. Liu, L. Song, J. Zhu, L. Gu, L. Liu, H. Zhao, Y. Li and D. Wang, *Nat. Chem.*, 2018, **10**, 924–931.

17 N. Yang, Y. Liu, H. Wen, Z. Tang, H. Zhao, Y. Li and D. Wang, *ACS Nano*, 2013, **7**, 1504–1512.

18 J. Yan, C. E. Ren, K. Maleski, C. B. Hatter, B. Anasori, P. Urbankowski, A. Sarycheva and Y. Gogotsi, *Adv. Funct. Mater.*, 2017, **27**, 1701264.

19 H. Wang, T. Maiyalagan and X. Wang, *ACS Catal.*, 2012, **2**, 781–794.

20 T. Akhter, M. M. Islam, S. N. Faisal, E. Haque, A. I. Minett, H. K. Liu, K. Konstantinov and S. X. Dou, *ACS Appl. Mater. Interfaces*, 2016, **8**, 2078–2087.

21 T. Lin, I.-W. Chen, F. Liu, C. Yang, H. Bi, F. Xu and F. Huang, *Science*, 2015, **350**, 6267.

22 Y. Xu, C. Y. Chen, Z. Zhao, Z. Lin, C. Lee, X. Xu, C. Wang, Y. Huang, M. I. Shakir and X. Duan, *Nano Lett.*, 2015, **15**, 4605–4610.

This journal is © The Royal Society of Chemistry and the Chinese Chemical Society 2019

Mater. Chem. Front., 2019, **3**, 1310–1316 | **1315**

23 Z. Teng, N. Yang, H. Lv, S. Wang, M. Hu, C. Wang, D. Wang and G. Wang, *Chem*, 2019, **5**, 1–17.

24 N. Yang and D. Wang, *Chem*, 2018, **4**, 2260–2277.

25 Q. Tang, Z. Zhou and P. Shen, *J. Am. Chem. Soc.*, 2012, **134**, 16909–16916.

26 M. Naguib, M. Kurtoglu, V. Presser, J. Lu, J. J. Niu, M. Heon, L. Hultman, Y. Gogotsi and M. W. Barsoum, *Adv. Mater.*, 2011, **23**, 4248–4253.

27 H. W. Wang, M. Naguib, K. Page, D. J. Wesolowski and Y. Gogotsi, *Chem. Mater.*, 2016, **28**, 349–359.

28 B. Anasori, M. R. Lukatskaya and Y. Gogotsi, *Nat. Rev. Mater.*, 2017, **2**, 16098.

29 X. Geng, Y. Zhang, Y. Han, J. Li, L. Yang, M. Benamara, L. Chen and H. Zhu, *Nano Lett.*, 2017, **17**, 1825–1832.

30 M. Acerce, D. Voiry and M. Chhowalla, *Nat. Nanotechnol.*, 2015, **10**, 313–317.

31 X. Cong, C. Cheng, Y. Liao, Y. Ye, C. Dong, H. Sun, X. Ji, W. Zhang, P. Fang, L. Miao and J. Jiang, *J. Phys. Chem. C*, 2015, **119**, 20864–20870.

32 Q. Tang and D. Jiang, *Chem. Mater.*, 2015, **27**, 3743–3748.

33 G. Kresse and J. Furthmüller, *Phys. Rev. B: Condens. Matter Mater. Phys.*, 1996, **54**, 11169–11186.

34 J. P. Perdew, K. Burke and M. Ernzerhof, *Phys. Rev. Lett.*, 1996, **77**, 3865.

35 M. Calandra, *Phys. Rev. B: Condens. Matter Mater. Phys.*, 2013, **88**, 245428.

36 J. Heising and M. G. Kanatzidis, *J. Am. Chem. Soc.*, 1999, **121**, 638–643.

37 H. L. Tsai, J. Heising, J. L. Schindler, C. R. Kannewurf and M. G. Kanatzidis, *Chem. Mater.*, 1997, **9**, 879–882.

38 F. Wypych and R. Schollhorn, *J. Chem. Soc., Chem. Commun.*, 1992, **19**, 1386–1388.

39 T. Hu, R. Li and J. Dong, *J. Chem. Phys.*, 2013, **139**, 174702.

40 M. Kan, J. Y. Wang, X. W. Li, S. H. Zhang, Y. W. Li, Y. Kawazoe, Q. Sun and P. Jena, *J. Phys. Chem. C*, 2014, **118**, 1515–1522.

41 K. E. Dungey, M. D. Curtis and J. E. P. Hahn, *Chem. Mater.*, 1998, **10**, 2152–2161.

42 X. Yang, L. Zhao and J. Lian, *J. Power Sources*, 2017, **343**, 373–382.

43 M. Wang, L. Fan, D. Tian, X. Wu, Y. Qiu, C. Zhao, B. Guan, Y. Wang, N. Zhang and K. Sun, *ACS Energy Lett.*, 2018, **3**, 1627–1633.

44 L. Wang, X. Zhang, Y. Ma, M. Yang and Y. Qi, *J. Phys. Chem. C*, 2017, **121**, 9089–9095.

45 J. Wang, D. Chao, J. Liu, L. Li, L. Lai, J. Lin and Z. Shen, *Nano Energy*, 2014, **7**, 151–160.

46 W. J. Tang, X. L. Wang, D. Xie, X. H. Xia, C. D. Gu and J. P. Tu, *J. Mater. Chem. A*, 2018, **6**, 18318–18324.

47 M. Khazaei, M. Arai, T. Sasaki, A. Ranjbar, Y. Liang and S. Yunoki, *Phys. Rev. B: Condens. Matter Mater. Phys.*, 2015, **92**, 075411.

48 N. Joseph, P. M. Shafi and A. C. Bose, *New J. Chem.*, 2018, **42**, 12082–12090.

49 C. Y. Zhao, J. M. Ang, Z. L. Liu and X. Lu, *Chem. Eng. J.*, 2017, **330**, 462–469.

50 R. Addou, L. Colombo and R. M. Wallace, *ACS Appl. Mater. Interfaces*, 2015, **7**, 11921–11929.

51 Z. Q. Fan, X. W. Jiang, J. W. Luo, L. Y. Jiao, R. Huang, S. S. Li and L. W. Wang, *Phys. Rev. B*, 2017, **96**, 165402.

52 W. Zhou, X. L. Zou, S. Najmaei, Z. Liu, Y. Shi, J. Kong, J. Lou, P. M. Ajayan, B. I. Yakobson and J. C. Idrobo, *Nano Lett.*, 2013, **13**, 2615–2622.

53 J. Hong, Z. Hu, M. Probert, K. Li, D. Lv, X. Yang, L. Gu, N. Mao, Q. Feng, L. Xie, J. Zhang, D. Wu, Z. Zhang, C. Jin, W. Ji, X. Zhang, J. Yuan and Z. Zhang, *Nat. Commun.*, 2015, **6**, 6293.